JOURNAL OF GEOPHYSICAL RESEARCH: SOLID EARTH, VOL. 118, 1304–1315, doi:10.1002/jgrb.50126, 2013

Fracture patterns in nonplane strain boudinage—insights from 3-D discrete element models

Steffen Abe,[1] Janos L. Urai,[1,2] and Michael Kettermann[1]

Received 30 April 2012; revised 21 November 2012; accepted 8 February 2013; published 28 March 2013.

[1] We use 3-D Discrete Element Method simulations to model the evolution of boudin structures in a layered material under nonplane strain conditions. As the models are shortened perpendicular to the layer orientation, they are extended at different rates in the two layer-parallel directions. The particular emphasis of the study is on the orientation of fractures between the boudin blocks. The results show that the fracture orientation distribution is closely connected to the ratio of the two layer-parallel extension rates. The anisotropy of the fracture orientation distribution increases systematically from no anisotropy at isotropic layer-parallel extension to a highly anisotropic distribution in case of uniaxial extension. We also observe an evolution of the anisotropy of fracture orientation distribution with increasing deformation in each individual model from a high-initial anisotropy towards a value characteristic for the ratio of the layer-parallel extension rates. The observations about the relation between the strain ratios and the fracture patterns do have the potential to serve as the basis for a new method to analyze strains in naturally boudinaged rocks.

Citation: Abe, S., J. L. Urai, and M. Kettermann (2013), Fracture patterns in nonplane strain boudinage—insights from 3-D discrete element models, *J. Geophys. Res. Solid Earth*, *118*, 1304–1315, doi:10.1002/jgrb.50126.

1. Introduction

[2] Boudins are relatively common structures in mechanically layered rocks that have been extended in a layer-parallel direction. They have been described in detail by, for example, *Ramberg* [1955], *Ramsay and Huber* [1987], *Twiss and Moores* [2007], and *Goscombe et al.* [2004]. The basic mechanisms governing the evolution of boudinage structures have been investigated by a wide range of numerical and analogue models [*Mandal and Khan*, 1991; *Bai and Pollard*, 1999; *Bai et al.*, 2000; *Mandal et al.*, 2000; *Passchier and Druguet*, 2002; *Li and Yang*, 2007; *Iyer and Podladchikov*, 2009; *Maeder et al.*, 2009; *Zulauf et al.* 2009, 2010; *Abe and Urai*, 2012] and are thought to be reasonably well understood. Based on this, the shape and orientation of the boudins is often seen as an indicator of the stress and strain or strain rate conditions that have been acting on the layered rocks at the time the boudins were formed [*Goscombe and Passchier*, 2003; *Maeder et al.*, 2009].

[3] Most information that is available about the geometry of boudins, particularly at the outcrop scale, is in 2-D. An overview over the wide range of boudin types observed in 2-D is given by *Goscombe et al.* [2004]. However, much less is known about the 3-D geometry of boudin structures. In some cases, the outcrop conditions are favorable enough to enable field observations of the boudin geometries in 3-D, for example, in the case of boudinaged pegmatites in a marble matrix [*Schenk et al.*, 2007] and in silicicalstic rocks exposed at the SW coast of Portugal [*Zulauf et al.*, 2011a]. More comprehensive 3-D data is available at the large scale from seismic images of boudinaged carbonate or anhydrite stringers in salt bodies [*van Gent et al.*, 2011; *Strozyk et al.*, 2012]. Additional information on the shape and the evolution of boudins in 3-D has been available recently from analogue experiments [*Zulauf et al.*, 2009, 2010, 2011b; *Kettermann*, 2009]. To gain additional insights into the range of boudin geometries expected in 3-D, we have performed a series of numerical experiments to study the influence of stress and strain conditions on the 3-D fracture patterns in boudinaged layers. The work is particularly focused on the investigation of the evolution of boudin structures under nonplane strain conditions because significant deviations from the 2-D models are expected.

2. Method

2.1. Discrete Element Model

[4] The numerical models used in this work are built by extending the 2-D boudinage models used by *Abe and Urai* [2012] to 3-D. The numerical simulation is based on the Discrete Element Model (DEM) initially developed by *Cundall and Strack* [1979] and extended by *Mora and Place* [1994], *Place and Mora* [1999], *Potyondy and Cundall*

[1]Structural Geology - Tectonics - Geomechanics, RWTH Aachen University, Templergraben, Aachen, Germany.
[2]Faculty of Science, German University of Technology (GUTech), Muscat, Sultanate of Oman.

Corresponding author: S. Abe, now at igem -Institut for Geothermal Resource Management, University of Applied Sciences Bingen, Berlinstr. 107a 55411, Bingen, Germany. (s.abe@ged.rwth-aachen.de)

2169-9313/13/10.1002/jgrb.50126

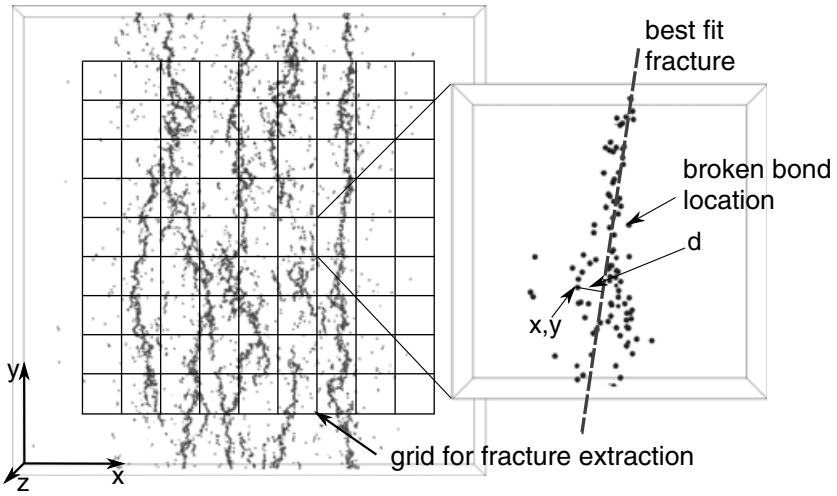

Figure 1. Determining the fracture orientations. The grid shown here is for illustration purposes. To improve the clarity of the figure, a larger grid spacing shown here is larger than the one used in the actual calculations. The x, y coordinates in the right plot are the position of the broken bond location pointed to and d is the distance between the broken bond and the best fit fracture.

[2004], and *Wang et al.* [2006]. In the Discrete Element Method, the material is modeled as a collection of spherical particles interacting with their nearest neighbors by frictional, brittle-elastic, quasi-viscous, or other interactions. In the case of brittle-elastic interactions or bonds, the interaction can "break" if a given failure criterion is fulfilled and be replaced by a frictional and repulsive elastic interaction. Using this mechanism, the brittle failure of cohesive materials is intrinsically included in the method [*Mora and Place*, 1994; *Potyondy and Cundall*, 2004]. In order to obtain realistic fracture behavior, we have used the particle bond implementation by *Wang et al.* [2006] taking normal, tangential, bending, and torsion forces into account. Ductile material is modeled using the "dash-pot" interactions between the particles described by *Abe and Urai* [2012] resulting in a "quasi-viscous" material behavior similar to Bingham plasticity [*Middleton and Wilcock*, 1994; *Twiss and Moores*, 2007]. To enable the simulation of large models with sufficient resolution even in 3-D, we have used the parallel DEM software ESyS-Particle [*Abe et al.*, 2003; *Weatherley et al.*, 2010, https://launchpad.net/esys-particle/].

2.2. Fracture Orientation Statistics

[5] To investigate the orientation of fractures in the boudinaged layer, we identify the locations of broken bonds in the model. The fracture locations are then projected into the x-y (i.e., layer-parallel) plane. The reason why we are restricting the analysis to two dimensions is that there is little variation in the fracture orientations in the third (z-) dimension. An indication of this can be seen in the cross sections in Figure 4 where the fractures are oriented mainly parallel to the z-axis. This is also compatible with the expectation that the fractures are predominantly tensile and therefore perpendicular to the layering.

[6] In a next step, the model area is decomposed into a square grid (Figure 1, left). A grid spacing of five model units was chosen, representing about 4% to 5% of the total model size in both layer-parallel directions that was either 100 model units for geometry "A" and 120 model units for geometry "B" (Table 1). For each grid cell, a line is determined that provides a "best fit" to the fracture locations (Figure 1, right) by minimizing the root-mean-square (RMS) distance between the fracture locations and the line. If there are too few broken bonds in a grid section or if the RMS distance between the best fit line and the fracture locations is too large, then it is assumed that there is no single consistent fracture orientation in this particular grid section and no orientation data is recorded. Based on the results of a number of tests, a threshold of 30 was chosen for the minimum number of broken bonds per grid cell. An RMS distance of one model unit, i.e., 20% of the grid spacing was used as threshold for the fit quality. One of the limitations of this approach is that the algorithm will return no orientation data for cases where multiple fractures cross the same grid cell. The orientations of the detected fracture segments are then combined into an angular distribution for which the statistical properties can be calculated.

[7] The outer part of the model space (i.e., outside the grid shown in Figure 1) is excluded from these calculations to avoid boundary effects, i.e., fractures always being perpendicular to a free surface.

[8] In order to quantify the anisotropy in the fracture orientation data, we tested three different methods: a Fourier transform approach, calculating a best fit ellipsis and the "fabric tensor" method. All three methods have their advantages and disadvantages as described below, but an evaluation has shown that the "fabric tensor" method is the most suitable one for the purpose of this work.

[9] A method for the determination of the anisotropy in orientation data suggested in the literature [*Rothenburg and Bathurst*, 1989] is to calculate the Discrete Fourier Transform (DFT) of the angular distribution of the orientations, i.e.,

$$h_i = \frac{1}{N}\left(\sum_{i=0}^{N-1} a_i \cos\left(\frac{2\pi i}{N}\right) + \sum_{i=0}^{N-1} b_i \sin\left(\frac{2\pi i}{N}\right)\right), \qquad (1)$$

Table 1. Geometric Parameters of the Model Realizations Used[a]

Geometry	l[b]	h[c]	r_{min}[d]	r_{max}[e]	n_p[f]	Models[g]
A	100	30	0.2	1.0	871,010	1–6
B	120	30	0.2	1.0	1,249,991	7–12
C	120	30	0.2	1.0	1,253,471	13–19

[a]All dimensions are in model units.
[b]The extension of the model in the two layer-parallel dimensions.
[c]Thickness of the model in the direction perpendicular to the layering.
[d]The minimum particle radius used.
[e]The maximum particle radius used.
[f]The number of particles in the model.
[g]Shows for which model runs each geometry was employed.

where h_i is the number of fractures that fall in the ith bin of the orientation histogram and N is the number of histogram bins. Due to the symmetry of the orientation distribution, only even Fourier components, i.e., a_{2i}, b_{2i} for $i = 0, \ldots, N/2$, are nonzero [*Rothenburg and Bathurst*, 1989]. The values of the "DC"-component of the DFT, i.e., a_0 in equation (1), and the the magnitude of the second Fourier component, i.e., $\sqrt{a_2^2 + b_2^2}$ in equation (1) can be used to calculate a measure A_F of the anisotropy of the orientation distribution as

$$A_F = \frac{\sqrt{a_2^2 + b_2^2}}{a_0} \quad . \tag{2}$$

[10] Tests with data from some of our models confirmed that the calculated anisotropy measure A_F is relatively robust with respect to the binning of the orientation histogram. Unfortunately, applying this approach to the fracture orientation data obtained from our simulations did also show that the fit between the measured data h_i and the approximation $h(\phi) = a_0 + a_2 \cos 2\phi + b_2 \sin 2\phi$ is not very good, in particular for strongly anisotropic distributions (Figure 2).

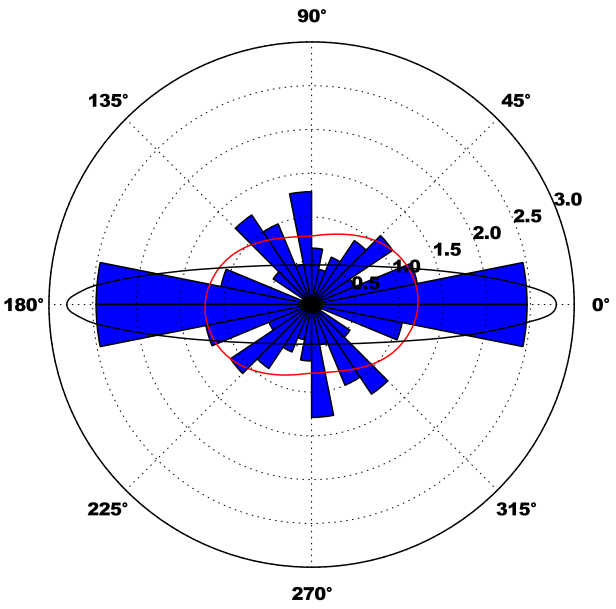

Figure 2. Histogram of orientation distribution (blue), best fit approximations based on the first 2 Fourier components (red) and best fit ellipse (black). The positive x-axis is oriented towards 0° and the positive y-axis towards 90°.

[11] An alternative would be to calculate a best fit ellipse and to use the ratio between the long axis r_l and the short axis r_s as a measure for the anisotropy.

$$h(\phi) = \sqrt{\frac{{r_s}^2}{1 - \epsilon^2 \cos(\phi)^2}}, \tag{3}$$

where ϵ is the numerical eccentricity of the ellipse. The axis ratio can then be calculated as

$$\frac{r_l}{r_s} = \frac{1}{\sqrt{1 - \epsilon^2}} \quad . \tag{4}$$

[12] While this results in a better fit for some data (Figure 2), tests did also show that the method has two major drawbacks. First, the anisotropy parameters obtained for a given orientation distribution show a significant dependence on the bin size of the orientation histogram used to calculate the ellipse. Additionally, the numerical optimization methods employed in the fitting process did not always converge, in particular if the orientation distributions were highly anisotropic.

[13] The "fabric tensor" has been used previously to determine the statistical properties of the distribution of particle contact directions in granular media [*Madadi et al.*, 2004; *Jerier et al.*, 2008]. We use a similar approach here for the orientation distribution of the fractures. The tensor F_{ij} is constructed the same way as described for the fabric tensor by *Madadi et al.* [2004], only that we are using the fracture directions instead of contact normals as input data. Therefore, the "orientation fabric tensor" is calculated as

$$F_{ij} = \frac{1}{n} \sum_{k=1}^{n} l_i^k l_j^k, \tag{5}$$

where n is the number of fractures considered and l_i^k and l_j^k are the ith and jth component of the kth direction vector l^k. Here the direction vector is a vector describing the orientation of one of the fracture segments found by the algorithm described at the beginning of the section (Figure 1). A measure of the anisotropy of the fracture orientation distribution can then be calculated from the ratio of the eigenvalues of the fabric tensor. As we are only considering the orientation of the fractures within the layer-parallel plane, the F_{ij} is a rank-2 tensor and therefore has two eigenvalues. Calculating the anisotropy coefficient A_T from the eigenvalues as

$$A_T = \frac{e_0 - e_1}{e_0}, \tag{6}$$

where e_0 is the larger and e_1 is the smaller of the two eigenvalues we get $A_T = 0$ for the isotropic case and $A_T = 1$ for complete anisotropy, i.e., if all fractures are aligned exactly in the same direction. A key advantage of this approach is that it does not involve the transformation of the fracture orientation data into a histogram, and the results are therefore not susceptible to a dependence on the choice of histogram bin size. However, unlike the DFT-based method described above, this approach is not able to detect the presence of higher-order components in the fracture orientation distribution.

2.3. Model Setup

[14] The models consists of a simple three-layer setup based on the 2-D models presented by *Abe and Urai* [2012]. In these models, a brittle central layer-oriented parallel to the *x*-*y* plane is embedded between two layers of ductile material. Interactions between particles belonging to the central brittle layer and the ductile matrix layers are described by a dashpot interaction, i.e., the layer interface is not welded and the drag exerted on the central layer by the two ductile layers is dependent on the slip rate at the layer interface.

[15] All models are square-shaped in the layer-parallel direction, i.e., the model dimensions in the *x*- and *y*-dimensions are the same. The boundary conditions in all three dimensions are formed by rigid plates interacting with the DEM particles by elastic forces (Figure 3). The top and bottom plates, i.e., those oriented parallel to the layering are servo-controlled to apply a defined normal stress of 0.005 model units to the model. Assuming a Young's modulus E = 20 GPa for the material, this would be equivalent to a normal stress of σ_n = 10 MPa. The four side boundary plates are displacement controlled. During the simulations, the side boundary plates are initially held stationary, while the normal stress on the top and bottom is linearly ramped up to the prescribed level. After this, the stress at top and bottom is held constant, and the side boundary plates are moved outwards. The velocity of the side plates is also increased linearly until the chosen strain rate is achieved and then held constant. This setup allows the precise control of the ratio between the layer-parallel strain components ϵ_{xx} and ϵ_{yy} during the simulations.

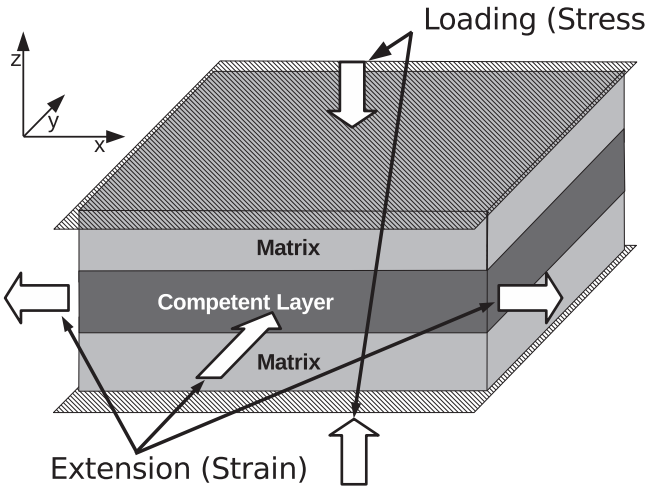

Figure 3. Schematic drawing of the general model setup. Matrix material is shown in light gray, the competent layer in dark gray, and the top and bottom rigid walls are drawn hatched. Side walls are not shown for clarity.

[16] All models are built using the similar basic geometry. The model thickness perpendicular to the layering is 30 model units. The central, competent layer has a thickness of 10 units. The model size in both layer-parallel dimensions is 100 or 120 model units. Using a minimum particle radius of 0.2 model units and a maximum particle radius of 1.0 model units, this results in a total of approximately 870.000 particles for the models with dimensions 100 × 100 × 30 model units and 1.2 million particles for the 120 × 120 × 30 models. The exact number varies slightly between the different random realizations of the particle packing (Table 1). Given that the ratio between particle radius and layer thickness mean that the brittle layer is only ≈10–20 particles thick, depending on the actual particle arrangement, the particles should not be seen as a direct representation of rock grains or even crystals but rather as the discretization of a larger volume of rock.

[17] Material properties were also adapted from the models by *Abe and Urai* [2012], i.e., the same microscopic interaction properties have been used. The cohesion of the brittle layer material is C = 0.0025 model units, making

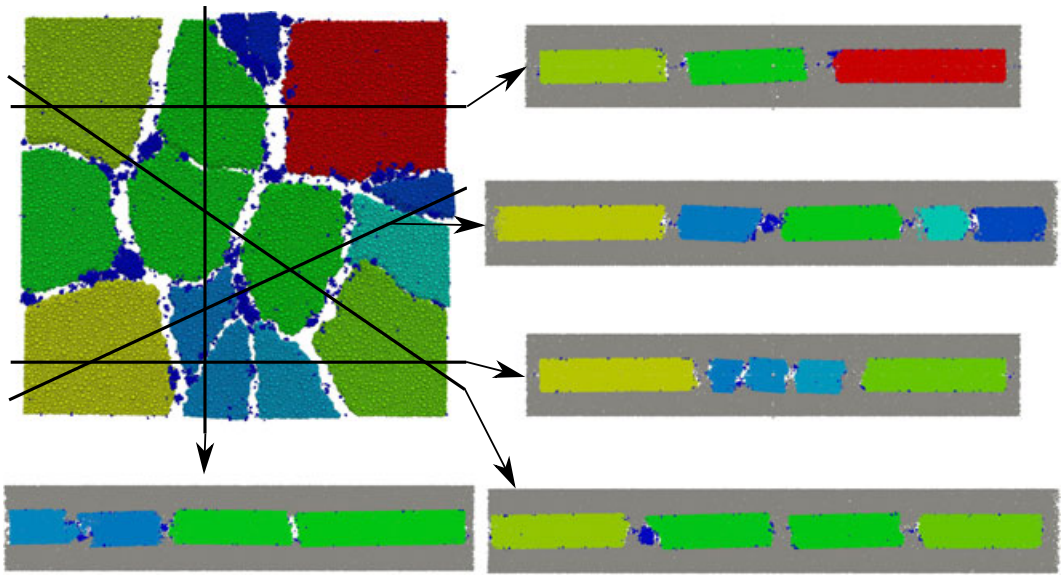

Figure 4. View of boudinaged brittle layer from the top, i.e., (top left) the +*z* direction as shown in Figure 3 and (right, bottom) cross-section profiles through the model (Model 19 in Table 2) along the lines shown. The gray material in the cross-section images are the ductile matrix layers.

the material properties similar to the intermediate strength models in *Abe and Urai* [2012]. Typical computing times for these models on current computer architectures (Intel Xeon 5675 cluster) are around 500 CPU hours (16–18 h on 30 cores) for small deformation models used to investigate the fracture orientation distribution and 2500 CPU hours for the simulations run to ≈20% extension (i.e., Figure 4).

Table 2. Model Parameters. The Details of the Model Geometries (column 2) Are Listed in Table 1. ϵ_{xx} and ϵ_{yy} Are the Final Extension Strains in *x*- and *y*-Direction

Model	Geometry	ϵ_{xx}	ϵ_{yy}	Strain Rate Ratio
1	A	0.069	0	1:0
2	A	0.0462	0.0154	1:0.33
3	A	0.0462	0.0231	1:0.5
4	A	0.0462	0.0462	1:1
5	A	0.0138	0.0092	1:0.66
6	A	0.0138	0.011	1:0.8
7	B	0.0231	0	1:0
8	B	0.0231	0.0076	1:0.33
9	B	0.0231	0.0116	1:0.5
10	B	0.0231	0.0152	1:0.66
11	B	0.0231	0.0185	1:0.8
12	B	0.0231	0.0231	1:1
13	C	0.0231	0	1:0
14	C	0.0231	0.0076	1:0.33
15	C	0.0231	0.0116	1:0.5
16	C	0.0231	0.0152	1:0.66
17	C	0.0231	0.0185	1:0.8
18	C	0.0231	0.0231	1:1
19	C	0.197	0.0985	1:0.5

3. Results

[18] In order to investigate the influence of the ratio between the extension rates in the two layer-parallel directions, a series of simulations were performed using strain ratios $\epsilon_{xx} : \epsilon_{yy}$ varying from uniaxial extension in *x*-direction and isotropic extension. To constrain the statistical variability of the results caused by the random particle packing used, each simulation with a given strain ratio was repeated for three realizations of the same basic model geometry using a different particle packing. The details of the models are listed in Table 2.

[19] The view of the boudinaged brittle layer parallel to the *x*-*y* plane shows either subparallel or polygonal fracture patterns, depending on the strain conditions (Figure 8, left column). Cross-section profiles perpendicular to the layering show 2-D boudinage structures similar to those observed in the pure 2-D models by *Abe and Urai* [2012] (Figure 4) even in models that show a polygonal fracture pattern in 3-D. The cross sections suggest that there is larger range of apparent boudin block sizes visible in the 2-D section through a set of polygonal 3-D boudins than would be

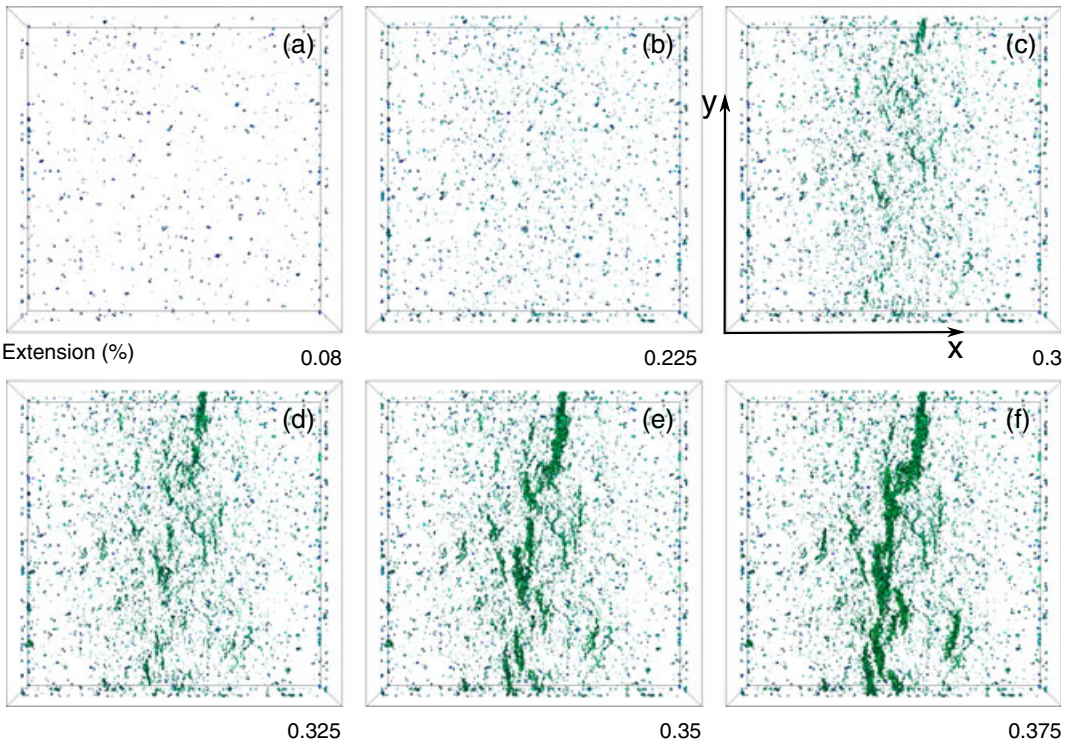

Figure 5. Crack formation by coalescence of microfractures in the early stages of deformation. Snapshots are taken from Model 2 (Table 2) using a strain ratio $\epsilon_{xx} : \epsilon_{yy} = 1 : 0.33$. The figures show the locations of the particle bonds broken at an extension in *x*-direction of (a) 0.08%, (b) 0.225%, (c) 0.3%, (d) 0.325%, (e) 0.35%, and (f) 0.375%. Colors show the timing of individual fractures, cold colors being early and warm colors being late. The outer boxes around the individual images show the outline of the whole model in a 3-D view.

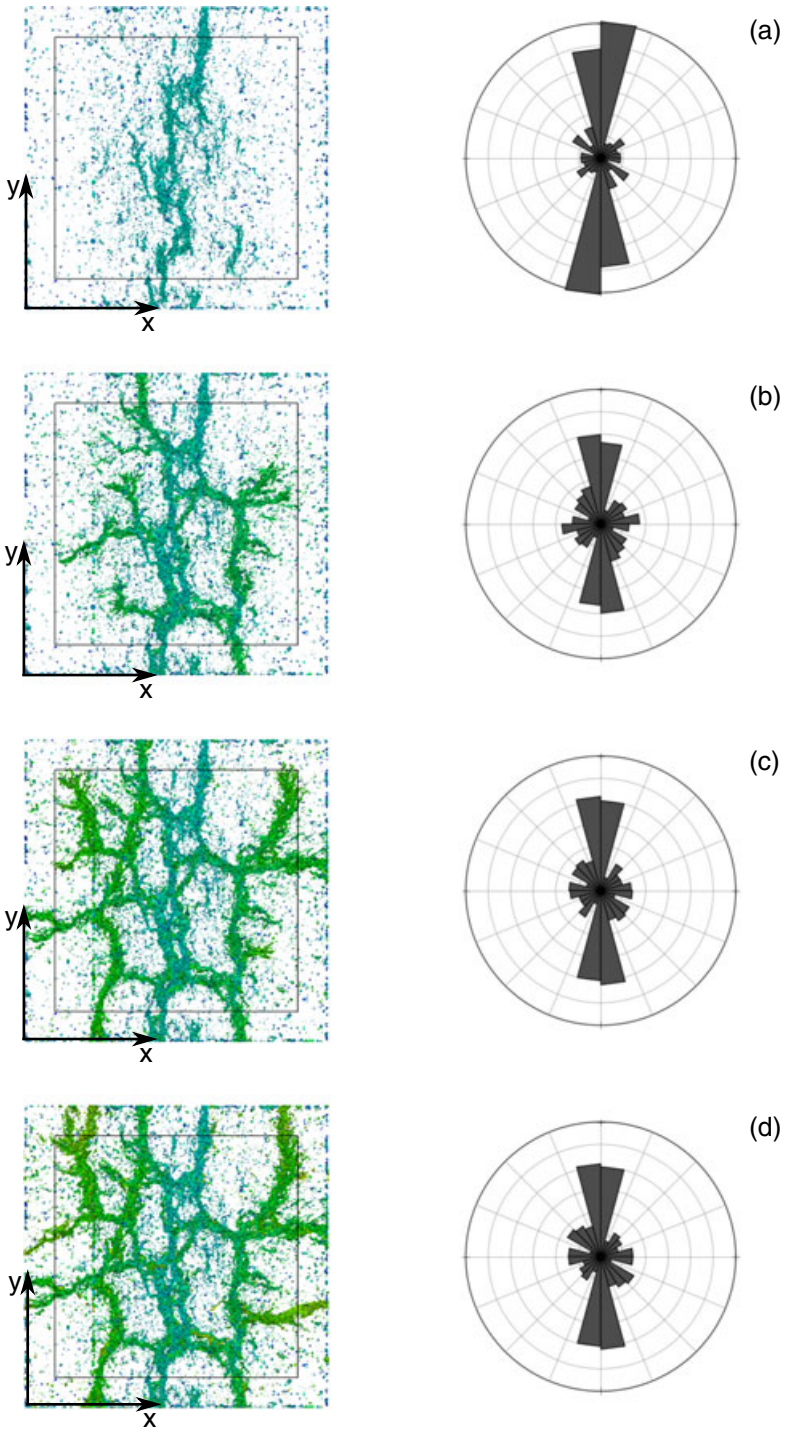

Figure 6. Evolution of the fractures in Model 3 (Table 2), using a ratio between the strain components of $\epsilon_{xx} : \epsilon_{yy} = 1 : 0.5$. Locations of broken bonds (left column) are colored by fracture time, cold colors being early and warm colors being late. The angular histograms of the fracture orientations are shown in the right column. Snapshots are taken at (a) $\epsilon_{xx} = 0.375\%$, (b) 0.625%, (c) 0.875%, and (d) 1.125%. The inner box in the images in the left column shows the part of the model that was used to extract the fracture orientations.

expected from a pure 2-D model or a 3-D plane strain model. This is caused be the possibility that in 3-D, a cross section is cutting some of the boudin blocks near their center so that the apparent block size in the direction along the cross section is similar to the true diameter of the block, but other blocks are cut closer to a corner so that the apparent block length visible in the cross section is much smaller than the real diameter of the intersected boudin block. However, due to the limited model size, there is no quantitative statistical evidence for this observation.

3.1. Evolution of Fracture Orientations During Progressive Deformation

[20] By extracting the time and location when the bonds between particles break, it is possible to observe in detail how the fracture patterns evolve with increasing strain. The results (Figure 5) show that in the initial phase of the deformation, the individual bond breaking events, which can be considered microcracks in a natural material, are distributed relatively evenly throughout the competent layer (Figure 5a and 5b). During the next stage of the deformation, some of those microcracks link up to form intermediate size fractures (Figure 5c and 5d) that finally coalesce into fractures spanning the whole model (Figure 5e and 5f). While Figure 5 shows only one example of this process, the observations are similar for all models investigated in the work. This process shows a strong similarity to observations of fracture growth in compression experiments on dolomitic marble by *Barnhoorn et al.* [2010], despite the applied stress and strain conditions being different.

[21] The fact that the major fractures in the model are generated by the merging of intermediate-sized fractures, which in many cases are not perfectly aligned but offset relative to each other, leads to the appearance of steps and relay structures along the main fractures. This, together with the mechanical heterogeneity of the model material caused by the random particle packing, provides an explanation why we observe mainly rough rather than straight fractures in our models.

[22] The evaluation of the fracture patterns evolving during further deformation of the model shows that the early macroscopic fractures are oriented predominantly perpendicular to the main extension direction (Figure 6a), except in models where no preferred direction exists, i.e., in case of isotropic extension. With increasing deformation, fractures start to form that are not perpendicular with the main extension direction, resulting in a network of randomly oriented fractures (Figure 6b–6d). The strain at which the fractures in the directions not perpendicular to the main extension directions start to appear is different between the models depending on the ratio. By this mechanism, the fracture orientation distribution changes from an initially highly anisotropic pattern that is not too dissimilar to that observed in uniaxial extension toward a less anisotropic pattern that is characteristic for the strain ratio in the model (Figure 6, right column).

[23] Calculating the degree of anisotropy in the fracture orientation distribution as described in section 2.2 during progressive deformation shows that there is a continuous decrease in anisotropy toward the final value (Figure 7). The large scatter of the anisotropy coefficient A_T during the early part of the deformation observed in some of the models, in particular the models with strain ratios 1:1 and 1:0.8 for strains $e_{xx} < 0.004$, is due to the low number of macroscopic fractures at this stage.

[24] Comparing the evolution of the anisotropy coefficient A_T for the models with different strain ratio $\epsilon_{xx} : \epsilon_{yy}$ in Figure 7 shows that the models with a smaller ratio between the strain components reach their characteristic "steady state" value of the fracture orientation anisotropy for less strain in the *x*-direction than those with a higher strain anisotropy. However, the strain in *y*-direction ϵ_{yy} at which the steady state value of A_T is reached is much more similar between the models, excluding the model with pure uniaxial extension. The strain in *y*-direction ϵ^A_{yy} at which the characteristic fracture anisotropy is reached is approximately $\epsilon^A_{yy} = \epsilon^A_{xx} = 0.0037$ for the anisotropic model, $\epsilon^A_{yy} = 0.0035$ for $\epsilon_{xx} : \epsilon_{yy} = 1 : 0.8$, $\epsilon^A_{yy} = 0.0041$ for $\epsilon_{xx} : \epsilon_{yy} = 1 : 0.66$, $\epsilon^A_{yy} = 0.0031$ for $\epsilon_{xx} : \epsilon_{yy} = 1 : 0.5$, and $\epsilon^A_{yy} = 0.0033$ for $\epsilon_{xx} : \epsilon_{yy} = 1 : 0.33$ (top left inset in Figure 7). These values suggest that the characteristic fracture anisotropy is reached when the extension in the direction with lower strain rate, i.e., in *y*-direction in this case, exceeds a critical value.

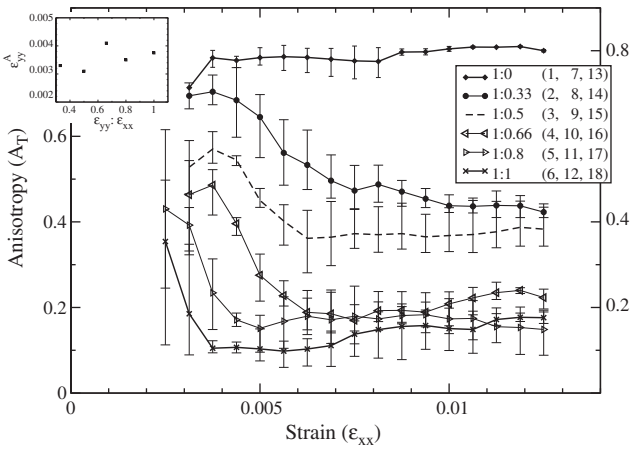

Figure 7. Evolution of the anisotropy of the fracture orientation distribution for increasing deformation. The error bars show minimum and maximum values, and the line shows the mean value. The anisotropy coefficient A_T is calculated according to equation (6). The numbers in the legend show the Model number as listed in Table 2. The inset on the top left shows the strain in *y*-direction ϵ_{yy} at which the characteristic fracture anisotropy is reached depending on the ratio between the strain components of $\epsilon_{xx} : \epsilon_{yy}$.

3.2. Fracture Orientations Versus Strain Ratio

[25] The investigation of the fracture evolution in section 3.1 did show that the characteristic fracture patterns stabilize at relatively small layer-parallel strains of $\epsilon_{xx} \leq 1\%$ (Figure 7). The final fracture patterns observed in the models are dependent on the ratio between the two layer-parallel strain components $\epsilon_{xx} : \epsilon_{yy}$ (Figure 8). We observe subparallel alignment of the fractures in case of uniaxial extension ($\epsilon_y = 0$) (Figure 8a) that is similar to that shown by *Kettermann* [2009] in analogue models. In the case of an isotropic extension parallel to the layer, i.e., $\epsilon_{xx} = \epsilon_{yy}$ (Figure 8d), the fracture patterns show a polygonal structure not unlike that observed in analogue models under similar strain conditions by *Kettermann* [2009] and *Zulauf et al.* [2009, 2010]. For intermediate ratios between ϵ_{xx} and ϵ_{yy}, the fracture patterns are polygonal, but the fragment shapes are elongated with the short dimension of the fragments being aligned with the direction of maximum extension of the layer (Figure 8b and 8c).

[26] As a measure of the shape of the boudin blocks, we have calculated the axis-aligned aspect ratio of the blocks in the final geometry of the different models. We are only

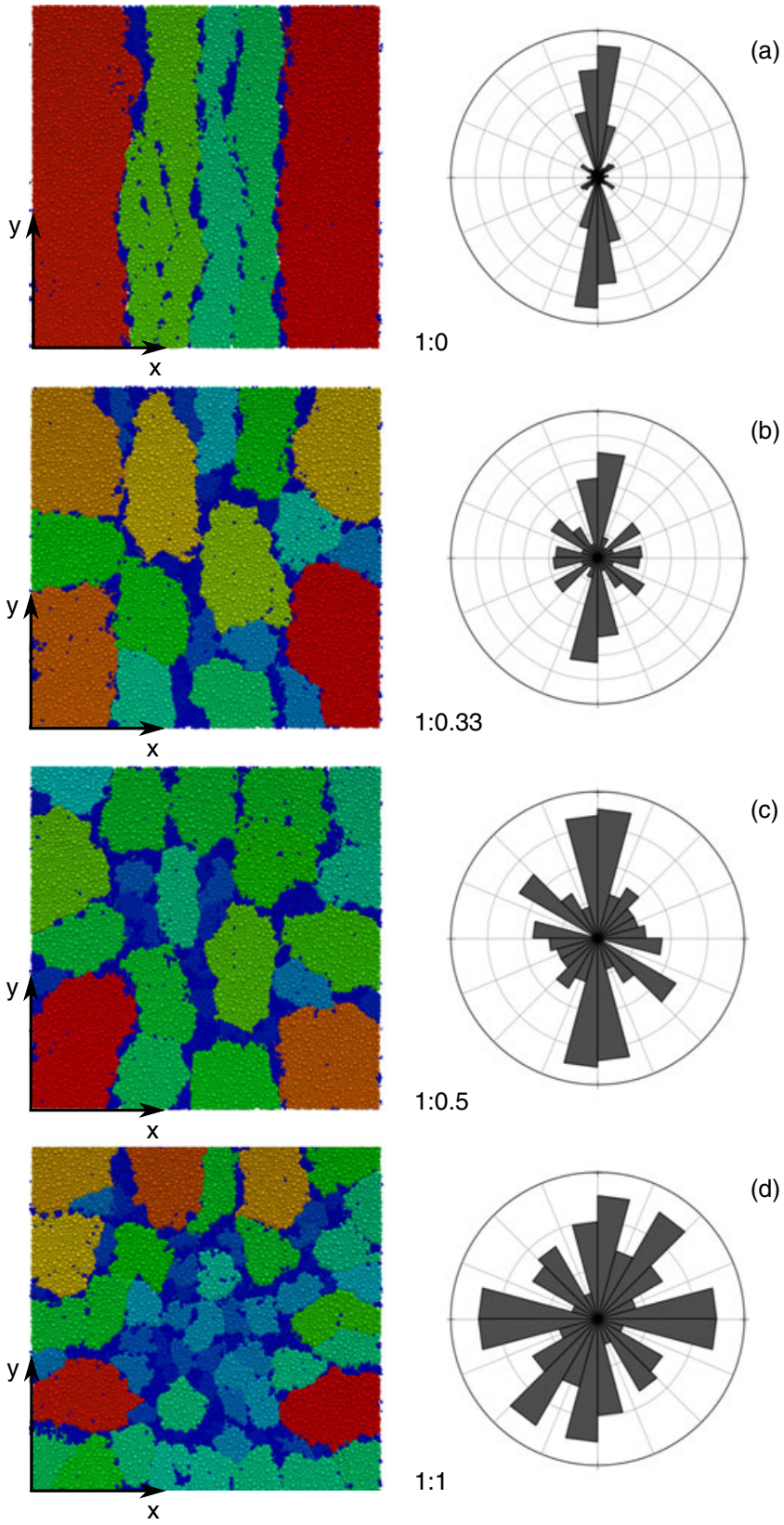

Figure 8. Characteristic fracture patterns of models with varying ratios between ϵ_{xx} and ϵ_{yy}. The left column shows the boudin blocks colored by block size, and the right column shows the orientation distribution of the fractures. The strain ratio $\epsilon_{yy} : \epsilon_{xx}$ is (a) 1:0 (uniaxial extension), (b) 1:0.33, (c) 1:0.5, and (d) 1:1 (isotropic extension). Model snapshots are taken at $\epsilon_{xx} = 0.023$.

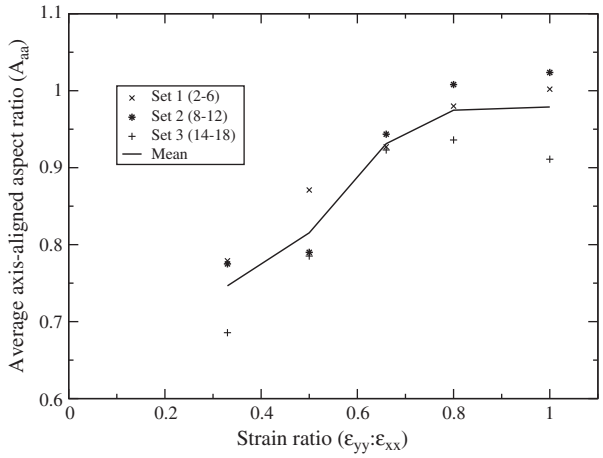

Figure 9. Average aspect ratio of the boudin blocks in models with varying ratios between ϵ_{xx} and ϵ_{yy}. Aspect ratio is calculated as $(x_{max} - x_{min})/(y_{max} - y_{min})$ for each boudin block. Model snapshots are taken at $\epsilon_{xx} = 0.023$. For the detailed parameters for model sets 1, 2, and 3, see Table 2.

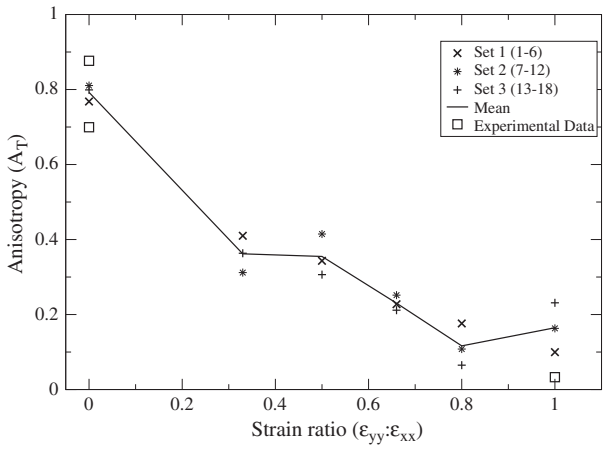

Figure 10. Anisotropy of the characteristic fracture orientation patterns depending on the strain ratio $\epsilon_{xx} : \epsilon_{yy}$. For the detailed parameters for model sets 1, 2, and 3, see Table 2. The experimental data are obtained from the laboratory experiments shown in Figure 11.

considering the layer-parallel dimension. The "axis-aligned" aspect ratio is defined here as the ratio between the maximum extension of the block in x- and y-direction, i.e., $A_{aa} = (x_{max} - x_{min})/(y_{max} - y_{min})$, not the ratio between the longest and the shortest dimension of the block. The values x_{min}, x_{max}, y_{min}, and y_{max} are the minimum and maximum extents of the block considered. They can be calculated from the particle center positions and the radii of all particle belonging to a particular block, i.e., $x_{min} = \min(x_i - r_i)$, where x_i is the x-positions of the center of particle i and r_i is its radius. The blocks at the model boundary have been excluded from the calculation to avoid boundary effects. Models 1, 7, and 18 (Table 2), i.e., the models with uniaxial extension, have been excluded because the y-dimension of the blocks in this model is determined by the model size, not by the fracturing process. Therefore, the aspect ratio of the blocks in those models is not comparable with those of the other models. The results show that the average aspect ratio of the fragments increases towards one, i.e., the block shapes becoming more equant with the strain ratio getting closer to one, i.e., the strain rates in x- and y-direction becoming more similar (Figure 9). However, this connection becomes weak for models approaching isotropic layer-parallel extension ($\epsilon_{yy}/\epsilon_{xx} \geq 0.8$).

[27] Using the methods described in section 2.2, the distribution of the fracture orientations in the final state of the models was investigated for $\epsilon_{xx} : \epsilon_{yy}$ ratios between 1:0 and 1:1. The results show that the orientation distribution of the fractures in the case of isotropic extension is parallel to the layers and the resulting fracture patterns are also isotropic (Figure 8d). The anisotropy coefficients calculated according to equation (6) are small at $A_T < 0.25$, i.e., there are no preferred fracture orientations. If the brittle layer is extended uniaxially, then the distribution of the fracture orientations is, as expected, strongly anisotropic (Figure 8a) with calculated anisotropy coefficients $A_T > 0.7$. However, the anisotropy does not reach the value $A_T = 1.0$ that would be predicted for perfectly parallel alignment of the fractures. This is due to the fact that the individual fractures between boudin blocks are not straight but have a finite roughness even in case of pure uniaxial extension. This is partially due to the heterogeneity of the material properties in the DEM model but also related to the fracture growth by coalescence as described in section 3.1.

[28] For models with intermediate ratios between ϵ_{xx} and ϵ_{yy} (Figure 8b and 8c), there is a relatively smooth transition from highly anisotropic fracture distributions at large $\epsilon_{xx} : \epsilon_{yy}$ ratios towards nearly isotropic distributions when the ratio is approaching $\epsilon_{xx} : \epsilon_{yy} \approx 1$ (Figure 10), i.e., there is no "threshold" value for the strain ratio where the fracture pattern jumps from predominantly subparallel fractures to an isotropic polygonal pattern but rather a gradual transition.

4. Discussion

[29] The fracture orientation distributions for the end-member models, i.e., uniaxial extension and layer-parallel isotropic extension are similar to those observed in the equivalent analogue experiments by *Kettermann* [2009]. These models consisted of a layer of brittle-cohesive material (hemihydrate powder) on top of a single layer of a viscous material (honey) (Figure 11a). During gravitational spreading of the viscous layer, a tensile stress is exerted on the brittle hemihydrate layer causing it to fracture. Despite the different boundary conditions, the fracture patterns (Figure 11, left) appear visually not too different from those generated in the numerical models (Figure 8, right). The fracture orientation histograms as shown in the right part of Figure 11 for the experiment and the right column of Figure 8 for the numerical models are also similar. Specifically, results of the experiments under uniaxial extension (Figures 11b and 11c) show similar fracture patterns to the numerical models under uniaxial extension (Figure 8a) and the fracture patterns in the experiment and the numerical models with isotropic extension (Figures 11d and 8d) are similar. The calculated anisotropy coefficients are also

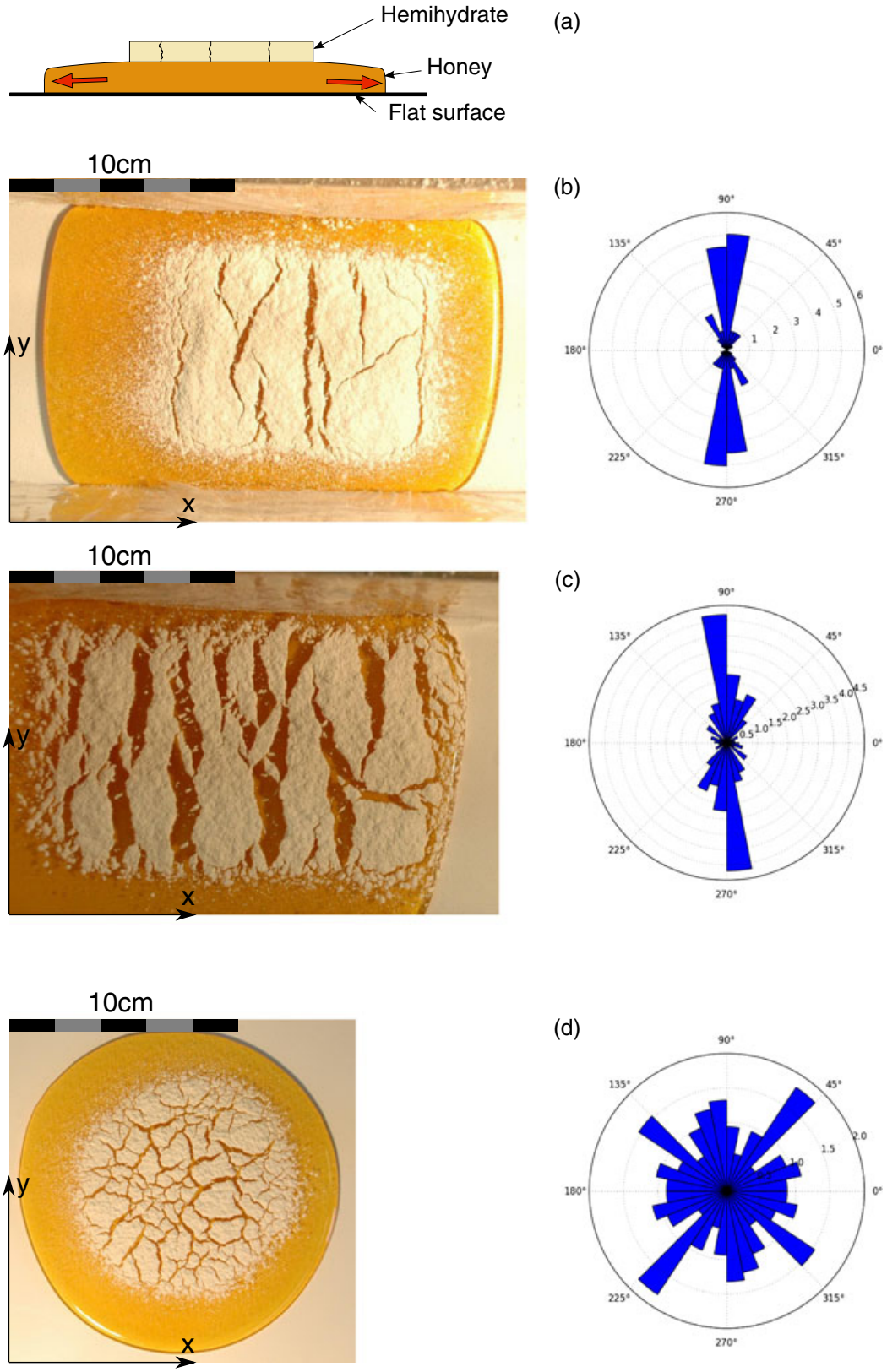

Figure 11. (a) Side view schematic drawing, (left) top view images of analogue boudinage experiments and (right) histograms of the fracture orientations observed in the experiments. (b and c) Shown are two realizations of uniaxial extension and (d) one experiment with radial, i.e., approximately isotropic, extension. Photographic images adapted from *Kettermann* [2009].

comparable. The value for the isotropic extension experiment is $A_T = 0.033$, while the value for the equivalent numerical models is $A_T = 0.10 – 0.23$. For the case of uniaxial extension, the values are $A_T = 0.70$ and $A_T = 0.88$ for the experiments and $A_T = 0.76 – 0.80$ for the numerical models.

[30] One feature of the numerical boudin models is that, as shown in Figure 8a, the fractures between the boudin blocks are rough rather than straight even in case of pure uniaxial extension. Due to the limited amount of information available about the three-dimensional geometry of natural boudins, it is not clear how common this feature is in nature. However, observations in analogue models suggest that the fractures between the boudin blocks are rough rather than straight in those experiments. See, for example, the models by *Kettermann* [2009] and Figure 3 in *Kidan and Cosgrove* [1996].

[31] These results might point towards a possibility to use the connection between the degree of anisotropy and the strain ratio as tool to constrain the deformation history of real 3-D boudins. Such a tool would be particularly useful in situations where the flow of the matrix material is complicated and spatially heterogeneous such as the 100 m–km scale boudinage of carbonate and anhydrite layers embedded in deformed salt bodies [*van Gent et al.*, 2011; *Strozyk et al.*, 2012]. However, further work will be needed to confirm the observed connection for real boudins. In particular, a comparison of the simulation results with data obtained from analogue models or possibly field data would be useful. Such comparisons would provide additional information to what extent the simplified material properties used in the DEM model are influencing the patterns formed in a boudinage process, for example, with respect to the fact the competent layer in the models used here is completely brittle, whereas some natural materials show ductile creep in addition to brittle failure.

[32] The polygonal fracture patterns for isotropic layer-parallel extension (pure flattening) and for models with intermediate strain ratios are always composed of random unevenly shaped polygons in our models that is consistent with observations from analogue models using similar strain conditions [*Kettermann*, 2009; *Zulauf et al.* 2009, 2010] . We do not observe a classic "chocolate tablet" boudinage dominated by two dominant perpendicular fracture directions as described by *Ghosh* [1988] and *Zulauf et al.* [2011b].

5. Conclusions

[33] The results of the study confirm that the Discrete Element Method (DEM) is a suitable tool for the numerical modeling of boudinage processes in 3-D. The comparison with the work of *Kettermann* [2009] shows that the models closely reproduce the boudinage patterns obtained in analogue models. While the computational costs are relatively high and the resolution of the models still remains below that of 2-D models, the works show that 3-D models are viable and do provide additional insights that could not be obtained from 2-D models alone.

[34] The two key results from the 3-D DEM modeling of boudinage are that (a) there is a clear connection between the strain ratio in the two layer-parallel dimensions and the anisotropy of the resulting fracture pattern and (b) the degree of fracture orientation anisotropy does evolve during increasing deformation until it reaches a value characteristic for a particular $\epsilon_{xx} : \epsilon_{yy}$ strain ratio.

[35] **Acknowledgments.** This study was carried out within the framework of DGMK (German Society for Petroleum and Coal Science and Technology) research project 718 "Mineral Vein Dynamics Modelling," which is funded by the companies ExxonMobil Production Deutschland GmbH, GDF SUEZ E&P Deutschland GmbH, RWE Dea AG, and Wintershall Holding GmbH, within the basic research program of the WEG Wirtschaftsverband Erdöl- und Erdgasgewinnung e.V. We thank the companies for their finacial support and their permission to publish these results.

[36] The main computations for this work were performed using the HPC cluster at RWTH Aachen University.

[37] We also thank the reviewers Elizabeth Ritz and Auke Barnhoorn and editor Tom Parsons for their helpful contributions.

References

Abe, S., and J. L. Urai (2012), Discrete element modeling of boudinage: Insights on rock rheology, matrix flow and evolution of geometry, *J. Geophys. Res.*, *117*, B01407, doi:10.1029/2011JB008555.

Abe, S., D. Place, and P. Mora (2003), A parallel implementation of the lattice solid model for the simulation of rock mechanics and earthquake dynamics, *Pure. Appl. Geophys.*, *161*(11–12), 2265–2277, doi: 10.1007/s00024-004-2562-X.

Bai, T., and D. D. Pollard (1999), Spacing of fractures in a multilayer at fracture saturation, *Int. J. Fracture*, *100*, L23—L28.

Bai, T., D. Pollard, and H. Gao (2000), Explanation for fracture spacing in layered materials, *Nature*, *403*, 753–755.

Barnhoorn, A., S. F. Fox, D. J. Robinson, and T. Senden (2010), Stress- and fluid-driven failure during fracture array growth: Implications for coupled deformation and fluid flow in the crust, *Geology*, *38*(9), 779–782, doi:10.1130/G31010.1.

Cundall, P. A., and O. Strack (1979), A discrete numerical model for granular assemblies, *Géotechnique*, *29*, 47–65.

Ghosh, S. (1988), Theory of chocolate tablet boudinage, *J. Struct. Geol.*, *10*(6), 541–553, doi:10.1016/0191-8141(88)90022-3.

Goscombe, B., and C. Passchier (2003), Asymmetric boudins as shear sense indicators–An assessment from field data, *J. Struct. Geol.*, *25*(4), 575–589, doi:10.1016/S0191-8141(02)00047-7.

Goscombe, B. D., C. W. Passchier, and M. Hand (2004), Boudinage classification: End-member boudin types and modified boudin structures, *J. Struct. Geol.*, *26*(4), 739–763, doi:10.1016/j.jsg.2003.08.015.

Iyer, K., and Y. Y. Podladchikov (2009), Transformation-induced jointing as a gouge for interfacial slip and rock strength, *Earth Planet. Sci. Lett.*, *280*, 159–166, doi:10.1016/j.epsl.2009.01.028.

Jerier, J.-F., D. Imbault, F. Donze, and R. Doremus (2008), A geometric algorithm based on tetrahedral meshes to generate a dense polydisperse sphere packing, *Granul. Matter*, *11*(1), 43–52, doi:10.1007/s10035-008-116-0.

Kettermann, M. (2009), The analogue modeling of boudins, BSc-Thesis, RWTH Aachen University.

Kidan, T., and J. Cosgrove (1996), The deformation of multilayers by layer-normal an experimental investigation, *J. Struct. Geol.*, *18*(4), 461–474

Li, Y., and C. Yang (2007), On fracture saturation in layered rocks, *Int. J. Rock Mech. and Min. Sci.*, *44*, 936–941, doi:10.1016/j.ijrmms.2006.11.009.

Madadi, M., O. Tsoungui, M. Lätzel, and S. Luding (2004), On the fabric tensor of polydisperse granular materials in 2D, *Int. J. Solid. Struct.*, *41*, 2563–2580, doi:10.1016/j.ijsolstr.2003.12.005.

Maeder, X., C. W. Passchier, and D. Koehn (2009), Modelling of segment structures: Boudins, bone-boudins, mullions and related single- and multiphase deformation features, *J. Struct. Geol.*, *31*(8), 817–830, doi: 10.1016/j.jsg.2009.05.13.

Mandal, N., and D. Khan (1991), Rotation, offset and separation of oblique-fracture (rhombic) boudins–Theory and experiments under layer-normal compression, *J. Struct. Geol.*, *13*(3), 349–356.

Mandal, N., C. Chakraborty, and S. K. Samanta (2000), Boudinage in multilayered rocks under layer-normal compression–A theoretical analysis, *J. Struct. Geol.*, *22*, 373–382.

Middleton, G. V., and P. R. Wilcock (1994), *Mechanics in the Earth and Environmental Sciences*, Cambridge University Press, Cambridge, U. K.

Mora, P., and D. Place (1994), Simulation of the frictional stick-slip instability, *Pure Appl. Geophys.*, *143*, 61–87.

Passchier, C. W., and E. Druguet (2002), Numerical modelling of asymmetric boudinage, *J. Struct. Geol.*, *24*(9), 1789–1803, doi:10.1016/S0191-8141(01)00163-8.

Place, D., and P. Mora (1999), The lattice solid model: Incorporation of intrinsic friction, *J. Int. Comp. Phys.*, *150*, 332–372.

Potyondy, D., and P. Cundall (2004), A bonded-particle model for rock, *Int. J. Rock Mech. and Min. Sci.*, *41* (8), 1329–1364, doi: 10.1016/j.ijrmms.2004.09.011.

Ramberg, H. (1955), Natural and experimental boudinage and pinch-and-swell structures, *J. Geol.*, *63*, 512–526.

Ramsay, J. G., and M. I. Huber (1987), *The Techniques of Modern Structural Geology*, Academic Press, London, U. K.

Rothenburg, L., and R. Bathurst (1989), Analytical study of induced anisotropy in idealized granular materials, *Géotechnique*, *39* (4), 601–614.

Schenk, O., J. L. Urai, and W. van der Zee (2007), Evolution of boudins under progressively decreasing pore pressure–A case study of pegmatites enclosed in marble deforning at high grade metamorphic conditions, Naxos, Greece, *Am. J. Sci.*, *307*, 1009–1033, doi:10.2475/07.2007.03.

Strozyk, F., H. van Gent, J. Urai, and P. A. Kukla (2012), 3D seismic study of complex intra-salt deformation: An example from the Upper Permian Zechstein 3 stringer, western Dutch offshore, in *Salt Tectonics, Sediments and Prospectivity, Special Publications*, edited by G. Alsop, S. Archer, A. Hartley, N. Grant, and R. Hodgkinson, vol. 363, Geological Society of London, pp. 489–501, London, U. K., doi:10.1144/SP363.23.

Twiss, R. J., and E. M. Moores (2007), *Structural Geology* second ed, W. H. Freeman and Company, New York.

van Gent, H., J. L. Urai, and M. de Keijzer (2011), The internal geometry of salt structures–A first look using 3D seismic data from the Zechstein of the Netherlands, *J. Struct. Geol.*, *33*, 292–311, doi: 10.1016.j.jsg.2010.07.005.

Wang, Y., S. Abe, S. Latham, and P. Mora (2006), Implementation of particle-scale rotation in the 3-D lattice solid model, *Pure Appl. Geophys.*, *163*, 1769–1785, doi:10.1007/s00024-006-0096-0.

Weatherley, D., V. Boros, W. Hancock, and S. Abe (2010), Scaling benchmark of eSyS-particle for elastic wave propagation simulations, in *Sixth IEEE International Conference on eScience*, pp. 277–283, Brisbane, Australia.

Zulauf, G., J. Zulauf, O. Bornemann, N. Kihm, M. Peinl, and F. Zanella (2009), Experimental deformation of a single-layer anhydrite in halite matrix under bulk constriction. Part 1: Geometric and kinematic aspects, *J. Struct. Geol.*, *31*, 460–474, doi:10.1016/j.jsg.2009.01.013.

Zulauf, G., J. Zulauf, O. Bornemann, F. Brenker, H. Höfer, M. Peinl, and A. Woodland (2010), Experimental deformation of a single-layer anhydrite in halite matrix under bulk constriction. Part 2: Deformation mechanisms and the role of fluids, *J. Struct. Geol.*, *32*(3), 264–277, doi: 10.1016/j.jsg.2009.12.001.

Zulauf, G., G. Gutierrez-Alonso, R. Kraus, R. Petschick, and S. Potel (2011a), Formation of chocolate-tablet boudins in a foreland fold and thrust belt: A case study from the external Variscides (Almograve, Portugal), *J. Struct. Geol.*, *33* (11), 1639–1649, doi: 10.1016/j.jsg.2011.08.009.

Zulauf, J., G. Zulauf, R. Kraus, G. Gutierrez-Alonso, and F. Zanella (2011b), The origin of tablet boudinage: Results from experiments using power-law rock analogs, *Tectonophysics*, *510*(3-4), 327–336, doi: 10.1016/j.tecto.2011.07.013.